

## Article

# Microstructure and Corrosion Resistance of Ti6Al4V Manufactured by Laser Powder Bed Fusion

Yiwa Luo <sup>1,\*</sup>, Mingyong Wang <sup>1</sup>, Jun Zhu <sup>2</sup>, Jiguo Tu <sup>1</sup> and Shuqiang Jiao <sup>1</sup>

<sup>1</sup> State Key Laboratory of Advanced Metallurgy, University of Science and Technology Beijing, Beijing 100083, China

<sup>2</sup> Ningxia Deyun Titanium Co., Ltd., Shizuishan 735000, China

\* Correspondence: lyw918@126.com

**Abstract:** Laser powder bed fusion (LPBF) technology has a dominant position in the preparation of titanium implants with a complex structure and precise size. However, the processing characteristics of rapid melting and solidification lead to the low density and poor corrosion resistance of the alloy. Hereby, the effects of the laser power and scanning rate on the density, hardness, compressive strength, and corrosion resistance of the Ti6Al4V alloy prepared by LPBF technology have been investigated by metallographic microscopy, a mechanical analysis, and electrochemical tests. The results show that increasing the scanning rate and decreasing the laser power decreases the transformation power from the  $\beta$  phase to  $\alpha'$  phase and changes the morphology of the  $\alpha'$  phase from lath shaped to acicular. The hardness of the Ti6Al4V alloy reaches the maximum (480.53 HV) for a scanning rate of 1000 mm/s and laser power of 280 W, owing to the sufficient precipitation of the  $\alpha'$  phase. Unfused holes occur in the titanium alloy when the laser energy density is too low to melt the powder. Pores occur when the laser energy density is too high to vaporize the powder. Both defects reduce the compressive strength of the alloy. The maximum relative density of the Ti6Al4V alloy is 99.96% for a scanning rate of 1200 mm/s and laser power of 240 W, and the compressive strength (1964 MPa) and corrosion resistance ( $3.16 \text{ M}\Omega\cdot\text{cm}^2$ ) both reached the maximum.



**Citation:** Luo, Y.; Wang, M.; Zhu, J.; Tu, J.; Jiao, S. Microstructure and Corrosion Resistance of Ti6Al4V Manufactured by Laser Powder Bed Fusion. *Metals* **2023**, *13*, 496. <https://doi.org/10.3390/met13030496>

Academic Editors: Antonello Astarita, Andrea El Hassanin, Alessia Teresa Silvestri and Marcello Cabibbo

Received: 27 December 2022

Revised: 10 February 2023

Accepted: 26 February 2023

Published: 1 March 2023



**Copyright:** © 2023 by the authors. Licensee MDPI, Basel, Switzerland. This article is an open access article distributed under the terms and conditions of the Creative Commons Attribution (CC BY) license (<https://creativecommons.org/licenses/by/4.0/>).

## 1. Introduction

According to the chemical composition and relative stabilities of the phases, titanium alloys can be divided into  $\alpha$ -Ti,  $(\alpha + \beta)$ -Ti, and  $\beta$ -Ti alloys. Ti6Al4V, as a type of medium strength  $\alpha + \beta$  titanium alloy, has been widely used in the medical sector due to its excellent mechanical properties, outstanding corrosion resistance, and biological performance [1–4]. Traditional technology to manufacture titanium alloy components with complicated shapes has the problems of low material utilization and a high cost. In recent years, additive manufacturing technology has been used to fabricate a complex titanium alloy medical assembly. Additive manufacturing (AM) technologies have been widely studied and applied in important areas, such as the aeronautic, astronautic, and medical fields, with minimum waste and excellent processing flexibility [5]. In contrast to traditional manufacturing, the obvious advantage of AM is that it can directly fabricate complex and internal characteristic components through line-by-line and then layer-by-layer processes from raw materials, without the need for secondary machining, while achieving an optimized mechanical performance, which cannot be accomplished by traditional processing methods [6]. Laser powder bed fusion (LPBF) is an increasingly applied 3D AM technology that integrates advanced laser technology, computer-aided design, manufacturing technology, and powder metallurgy technology. Compared with traditional processing methods, LPBF omits the manufacturing process of the mold, which has a great advantage in producing complex shapes and personalized components [7–10].

Generally, the quality of AM components is not ideal due to the micro-cracking and residual stresses, which restrict the use of these parts in applications with high tolerance and high fatigue strength requirements [11–13]. These shortcomings will endanger the mechanical performance, as well as the corrosion resistance. It has been shown that AM process parameters greatly influence the microstructure and mechanical properties of titanium alloys. The process parameters of LPBF are complex, including the laser power, scanning rate, layer thickness, and scanning spacing. These process parameters interact and have a great influence on the microstructure and mechanical properties of the titanium alloy, as well as a direct influence on the corrosion resistance of the material [14–16]. Among these parameters, the laser power and scanning rate are the most closely related to the microstructure and properties of the alloy. Edwards et al. [17] compared the fatigue properties of the Ti6Al4V alloy formed by LPBF with that of the forged titanium alloy and found that the fatigue life of the Ti6Al4V alloy formed by LPBF was smaller, which was related to the microstructure and density of the Ti6Al4V alloy. Dai et al. [18] studied the corrosion behavior of the Ti6Al4V alloy and GR5 titanium alloy formed by LPBF in normal saline. They found that the microstructure of the GR5 titanium alloy was composed of the typical  $\alpha + \beta$  phase, while the Ti6Al4V alloy was composed of a large amount of acicular martensite and less primary  $\beta$  phase. Thus, the corrosion resistance of the Ti6Al4V alloy was lower than that of the GR5 titanium alloy. Vandenbroucke et al. [19] explored the effect of the LPBF process parameters on the microstructure of the Ti6Al4V alloy. The results showed that when the laser power was 95 W and the scanning rate was 125 mm/s, the maximum density of the alloy was 99.8% and the hardness reached 410 HV. Song et al. [20] pointed out that the hardness of the Ti6Al4V alloy increased to 450 HV under the LPBF process with a laser power of 110 W and a scanning rate of 400 mm/s. Li et al. [21] investigated the microstructure and mechanical properties of the Ti6Al4V alloy manufactured by self-developed laser rapid-prototyping equipment. The results showed that the microstructure of the Ti6Al4V alloy was most uniform with a laser power of 2.5 kW and a scanning rate of 10 mm/s.

Ren et al. [22] reported that an appropriate scanning speed can not only increase the density of Ti-23Nb alloys but also improve its wear and corrosion resistance. The specimen produced at 2.6 mm/s possesses a lower corrosion potential ( $E_{corr}$ ) value owing to the presence of more  $\alpha''$  phase. Grain size is a critical factor in determining the corrosion current density ( $i_{corr}$ ). The high scanning speed specimen with small grain sizes has a high resistance and low corrosion current density. Jiang et al. [23] produced a ferritic stainless steel by LPBF at scanning speeds ranging from 2300 to 2700 mm/s and found that a scanning speed of 2300 mm/s produced materials with the lowest wear rate and corrosion current density [24]. In order to utilize the low cost and flexibility afforded by the powder mixture, a comprehensive understanding of the relationship between the laser parameter and microstructure evolution is required. Furthermore, the effect of the LPBF process on the corrosion resistance of titanium alloy in body fluids remains unclear.

Here, LPBF technology was used to investigate the influence of the scanning rate and laser power on the microstructure, mechanical properties, and corrosion resistance of the Ti6Al4V alloy. In addition, the mechanism was investigated at the microscale to achieve the regulation of the mechanical properties and corrosion resistance of the Ti6Al4V alloy. Moreover, the mechanical properties consisting of the Vickers hardness and compression behavior were analyzed. This work lays a solid foundation for the wide application of the Ti6Al4V alloy to reduce internal defects and improve the manufacturing efficiency.

## 2. Materials and Methods

### 2.1. Fabrication of Ti6Al4V by LPBF

The experimental equipment used for Ti6Al4V alloy preparation was an LPBF (EOS-M290, EOS, Berlin, Germany) system equipped with a 400 W Yb fiber laser. The diameter of the laser beam was 10  $\mu\text{m}$  and the shielding gas was 99.99% argon. The raw material was spherical Ti6Al4V alloy powder with an average particle size of 40  $\mu\text{m}$  which was

obtained by electrowinning according to the patent No. US11180863B2, and its chemical composition (mass fraction, %) was Al 5.67, V 4.21, O 0.12, C 0.01, H 0.001, Fe 0.1, and Ti balance. The scanning interval was 50  $\mu\text{m}$ ; the layer thickness was 30  $\mu\text{m}$ ; the laser power was 160 W, 200 W, 240 W, and 280 W; and the scanning rate was 1000 mm/s, 1200 mm/s, and 1400 mm/s. Before additive manufacturing, the Ti6Al4V powder was dried in an inert gas heater at 200 °C to remove the moisture. Metallographic and compression specimens with dimensions of 8 mm (diameter)  $\times$  15 mm (length) and samples for electrochemical measurement with dimensions of 1 mm  $\times$  5 mm  $\times$  10 mm were prepared.

## 2.2. Material Characterization

The metallographic specimens were polished and then corroded with Kroll etching solution ( $\text{HF:HNO}_3:\text{H}_2\text{O} = 1:3:7$  volume ratio). The microstructures of the specimens were observed with an optical microscope (OM, DM4M, Leica, Wetzlar, Germany). The densities of the samples were calculated by Image-Pro Plus software (version 6.0.0.260, Media Cybernetics Inc., Rockville, MD, USA). A Vickers hardness tester (VMHT30M, Leica, Wetzlar, Germany) was used to measure the surface hardness of the samples. The test was carried out for 10 s under 4.9 N. An electronic universal testing machine (CMT5150, Xinsansi, Shanghai, China) was used to measure the mechanical properties of the compression specimens. The strain rate was 0.005  $\text{s}^{-1}$  and each group of data was the average of five measured specimens. Each group of data is the average of 5 measured specimens. A composite lubricant of nickel anti-seize and tantalum foil (thickness of about 0.1 mm) is attached to the contact surface between the specimen and the anvils to minimize friction effects during hot deformation. Eliminate piston clearance after deformation temperature is reached to prevent buckling.

## 2.3. Electrochemical Tests

In order to investigate the corrosion resistance of Ti6Al4V implants in the biological environment, an electrochemical workstation equipped with the three-electrode system was used to perform the electro-chemical tests in the simulated body fluid (SBF). In the electrochemical test, the working electrode is the studied alloys with an exposed area of 1  $\text{cm}^2$ , the counter electrode was the platinum sheet, and the reference electrode was the saturated calomel electrode (SCE). The concentrations of the ions in SBF were  $\text{Na}^+$  142.0,  $\text{K}^+$  5.0,  $\text{Mg}^{2+}$  1.5,  $\text{Ca}^{2+}$  2.5,  $\text{Cl}^-$  147.8,  $\text{HCO}_3^-$  4.2,  $\text{HPO}_4^{2-}$  1.0, and  $\text{SO}_4^{2-}$  0.5 mM. The system was placed in a thermostatic water bath and kept at 37 °C for 24 h. The potentiodynamic polarization measurements were conducted at a scanning rate of 0.5 mV/s, ranging from -1 V to 1 V. The self-corrosion potential and corrosion current density were analyzed at the same time.

## 3. Results and Discussion

### 3.1. Influence of Laser Power and Scanning Rate on the Density and Microstructure of Ti6Al4V Alloy

The factors affected by the technological parameters in the LPBF forming process are relatively complex. During the forming process of the LPBF, the high-energy-density laser beam acts on the powder in the form of a body heat source. Therefore, the influence of the laser power and scanning rate on the forming thermodynamics of the specimen can be characterized by the laser energy density ( $E_v$ ) [25]:

$$E_v = \frac{P}{v \times L \times S} \quad (1)$$

where  $P$  is the laser power (W),  $v$  is the laser scanning rate (mm/s),  $L$  is the thickness of the alloy powder (mm), and  $S$  is the scanning interval (mm).

The variation in the density and laser energy density of the titanium alloy with a different laser power and scanning rate is shown in Figure 1. It can be seen that when the scanning rate is fixed, the increase in the laser power will cause the laser energy density

to increase continuously. Under the same laser power, the laser energy density decreases with the increase in the scanning rate. At the same time, it can be seen that when the scanning rate is 1400 mm/s, the density of the samples increases with the increase in the laser energy density. When the scanning rate was 1000 or 1200 mm/s, the density of the specimens showed a peak, and the morphology of the specimen at the peak showed a uniform structure and fewer porosity defects, as shown in Figure 1a. It is suggested that when  $E_v$  is higher than 155.55 J/mm<sup>3</sup>, the input energy of the titanium alloy powder results in severe convection in the micro-molten pool and the vaporization of the liquid alloy, forming round pores, as shown in Figure 1b. Gao et al. [26] also believe that the circular pore defect caused by powder gasification is the main reason for the low density of the parts when the laser energy is high. When  $E_v$  is lower than 76.19 J/mm<sup>3</sup>, the energy of the micro-molten pool is not sufficient to completely melt the titanium alloy powder. The high viscosity of the molten metal leads to the formation of the irregular shape of the incomplete defects, as shown in Figure 1c. These two types of pore defects both affect the mechanical properties of the sample.

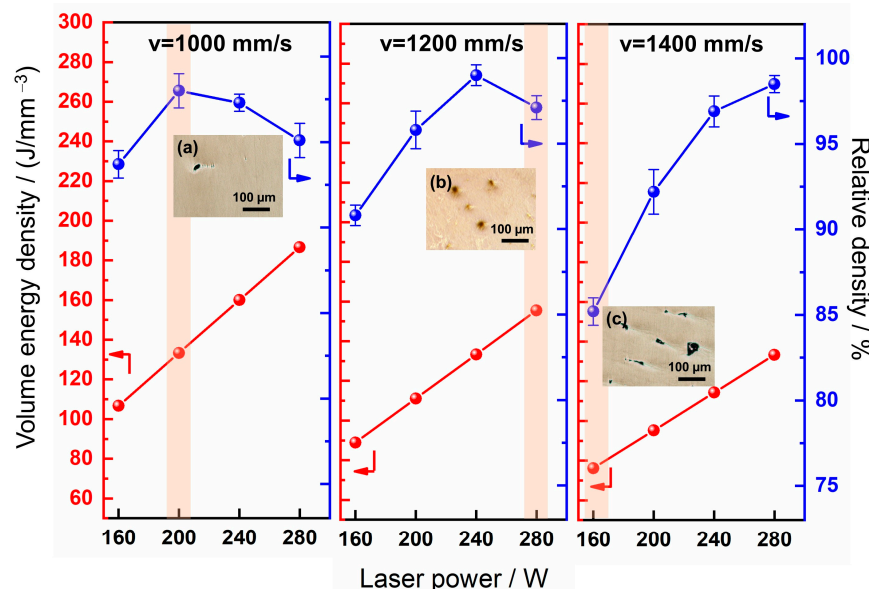


**Figure 1.** Volume energy density and relative density of Ti6Al4V alloy for different laser power and scanning rate. The inserts show metallographs of the specimens at (a)  $v = 1000 \text{ mm/s}$ ,  $P = 200 \text{ W}$ ; (b)  $v = 1200 \text{ mm/s}$ ,  $P = 280 \text{ W}$ ; and (c)  $v = 1400 \text{ mm/s}$ ,  $P = 160 \text{ W}$ .

Consequently, the increase in the laser energy density strengthens the fluidity and improves the density of Ti6Al4V. With a continuous increase in the laser energy density, it is easy to produce circular pores and decrease the density of the alloy. In contrast, a low laser energy density leads to the appearance of the incomplete penetration of the pore defects, resulting in a decrease in the density of the Ti6Al4V alloy. In this experiment, the maximum density of the titanium alloy was 99.96% at a scanning rate of 1200 mm/s and laser power of 240 W.

The metallographs of the Ti6Al4V alloy produced with a different laser power and scanning rate are shown in Figure 2. The microstructure of the samples consisted of the acicular  $\alpha'$  phase and a small amount of the  $\beta$  phase. Considering that the principle of the LPBF process is layer-by-layer superposition to form a repeated heating cycle and waste heat transformation, the matrix contained unfused  $\beta$  columnar crystals and acicular  $\alpha'$  martensite. The heat output increases with an increasing laser power, which enhances the transformation of the  $\beta$  phase to the  $\alpha'$  phase, resulting in a more extensive transformation of the  $\beta$  phase and the disappearance of the grain boundary (Figure 2a,b). The heating time of the alloy powder is prolonged under a slow scanning rate and is easier to form the acicular  $\alpha'$  phase. When the scanning rate increases, the increase in the cooling rate leads

to the incomplete transformation of the  $\beta$  phase to the  $\alpha'$  phase, resulting in a decrease in the acicular  $\alpha'$  phase (Figure 2c,d). Previous studies have shown that with an increasing cooling rate, the nucleation mechanism of the  $\alpha'$  phase changes from short-range diffusion to the shear mode [27,28]. In this study, a similar conclusion was obtained, where increasing the scanning rate changed the precipitation mechanism of the  $\alpha'$  phase, and the structure of the  $\alpha'$  phase changed from lath shaped to needle shaped (Figure 2e,f).

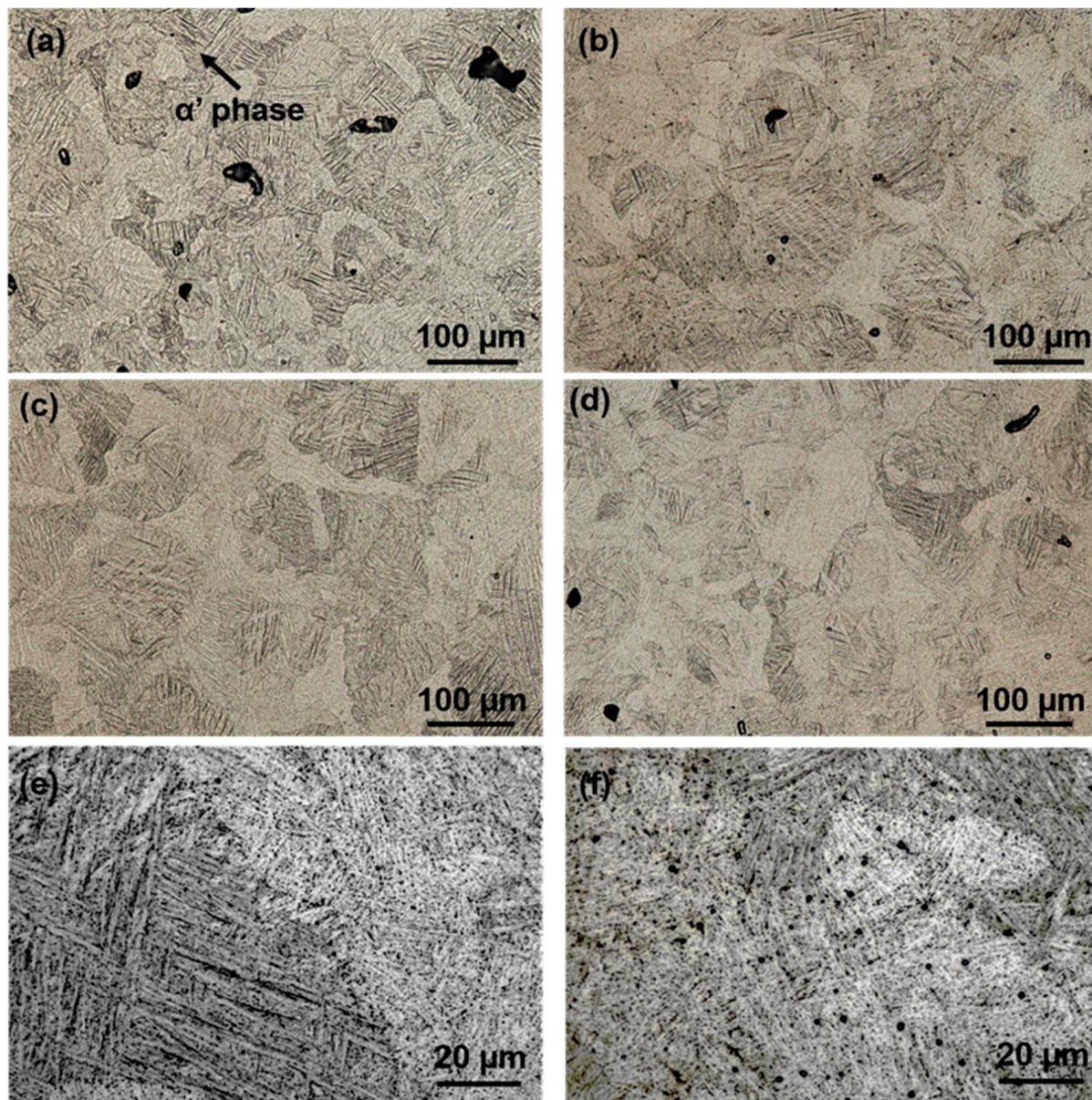


**Figure 2.** Metallographs of Ti6Al4V alloy prepared with the process parameter of (a)  $v = 1200 \text{ mm/s}$ ,  $P = 160 \text{ W}$ , (b)  $v = 1200 \text{ mm/s}$ ,  $P = 280 \text{ W}$ , (c)  $v = 1000 \text{ mm/s}$ ,  $P = 200 \text{ W}$ , (d)  $v = 1400 \text{ mm/s}$ ,  $P = 200 \text{ W}$ , and SEM micrographs of the Ti6Al4V alloy prepared with the process parameter of (e)  $v = 1000 \text{ mm/s}$ ,  $P = 200 \text{ W}$ , and (f)  $v = 1400 \text{ mm/s}$ ,  $P = 200 \text{ W}$ .

### 3.2. Influence of Laser Power and Scanning Rate on the Mechanical Properties of Ti6Al4V Alloy

The average hardness values of the Ti6Al4V alloy prepared with different laser power and scanning rates are shown in Figure 3. The hardness of the Ti6Al4V alloy increases with an increasing laser power at the scanning rate, and the maximum hardness value is 480.53 HV (280 W, 1000 mm/s). The hardness of the Ti6Al4V alloy decreases with an increasing scanning rate at the same laser power, and the minimum hardness value is 305.90 HV (160 W, 1400 mm/s). The titanium alloy powder undergoes repeated heating in the process of melting and reforming. A high laser power input slows down the residual heat emission and promotes the precipitation of the  $\alpha'$  phase. The acicular martensite structure of the  $\alpha'$  phase contributes to the improvement in the hardness. Conversely, the heating time and the total heat input of the micro-molten pool decrease with an increasing scanning rate, which is adverse for the precipitation of the  $\alpha'$  phase and reduces the hardness of the Ti6Al4V alloy.

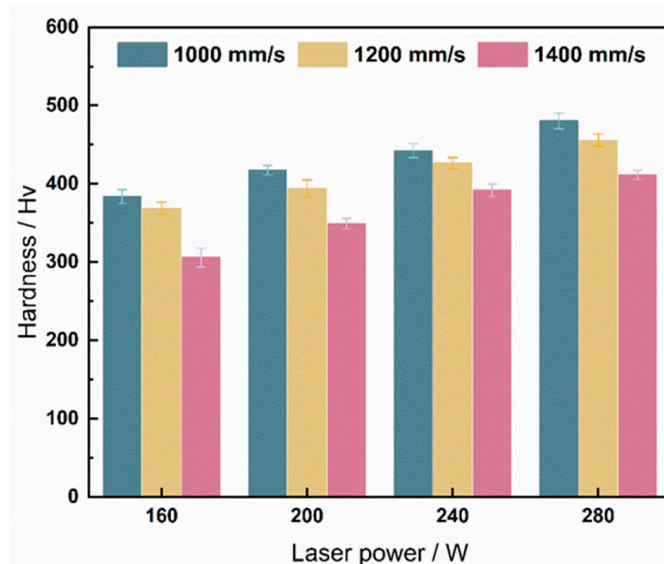


**Figure 3.** Vickers hardness of Ti6Al4V alloy prepared with different LPBF parameters.

The compressive strength values of the specimens prepared with different laser power and scanning rates, as well as the relationship between the density and compressive strength, are shown in Figure 4. The failure in the compression behavior of the Ti6Al4V alloy manufactured by LPBF is mainly caused by internal defects [29,30]. In general, the defects in additive manufacturing specimens mainly include pores, unfused holes, and cracks. Unfused holes occur in the titanium alloy when the laser energy density is low and the powder is not completely melted. Pores occur when the laser energy density is high and the powder is vaporized. The compressive strength of the Ti6Al4V alloy shows the same trend with the relative density. When the scanning rates are 1000 mm/s and 1200 mm/s (Figure 4a), the compressive strength of the specimen shows a trend of first increasing and then decreasing with the increase in the laser power. When the scanning rate is 1400 mm/s, the compressive strength of the specimen increases with an increasing laser power. The reason is that the hexagonal  $\alpha'$  phase is densely arranged with a strong interatomic bonding force, which is higher than that of the  $\beta$  phase. There is a direct proportional relationship between the density and the compressive strength (Figure 4b). When the density increases from 85.2% to 92.2%, the compressive strength of the titanium alloy increases significantly, and as the density keeps increasing, the compressive strength growth of the titanium alloy slows down.

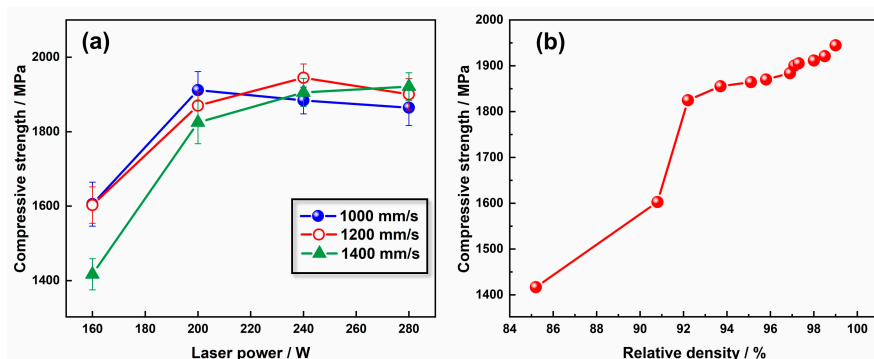


**Figure 4.** (a) Compressive strength of Ti6Al4V alloy and (b) the relationship between the compressive strength and the relative density.

### 3.3. Influence of Laser Power and Scanning Rate on the Corrosion Resistance of Ti6Al4V Alloy

The potentiodynamic polarization curves of the Ti6Al4V alloy manufactured by LPBF in SBF are shown in Figures 5 and 6. Usually, the corrosion current density ( $I_{corr}$ ) and self-corrosion potential ( $E_{corr}$ ) are used as important parameters to evaluate the corrosion resistance of materials, in which the corrosion current density determines the corrosion rate of the material [31]. The obtained  $I_{corr}$  and  $E_{corr}$  values are shown in Tables 1 and 2. From the corrosion thermodynamics perspective, it can be seen from Figure 5 that the  $E_{corr}$  value gradually increases with the increase in the laser power at the range of 160 W to 240 W, implying that the anodic corrosion tendency of Ti6Al4V alloys gradually reduces. From a corrosion kinetics perspective, the corrosion resistance derived from the  $I_{corr}$  exhibited a similar corrosion behavior with that obtained from the  $E_{corr}$ . As the laser power increased from 160 W to 240 W, the increasing laser energy density and heat input promote the formation of the anisotropic  $\alpha'$  acicular martensite and homogenize the microstructure, which inhibits the corrosion by the electrolyte and enhances the corrosion resistance of the specimen. Moreover, the grain size is a critical factor affecting the corrosion behavior [32]. The passivation ability correlates with active sites on the alloy surface, and a high density of the grain boundaries can promote the formation of passive films. Ralston et al. [33] established a Hall–Petch kind of relationship between the  $I_{corr}$  and the average grain size, which means that a decreased grain size leads to a reduction in the  $I_{corr}$ . When the laser power is increased to 280 W, the density of the Ti6Al4V alloy decreased, making it easier to cause pitting corrosion. The self-corrosion potential of the sample decreased, and the corrosion rate increased. The  $R_p$  value is the largest when the laser power is 240 W, i.e., approximately  $3.16 \text{ M}\Omega\cdot\text{cm}^2$ , indicating that the corrosion resistance is the best. This is consistent with the analysis results of the polarization curve.

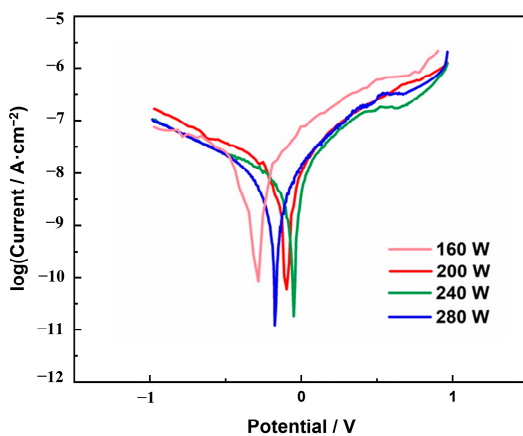


**Figure 5.** Polarization curves of Ti6Al4V alloy at scanning rate of 1200 mm/s.

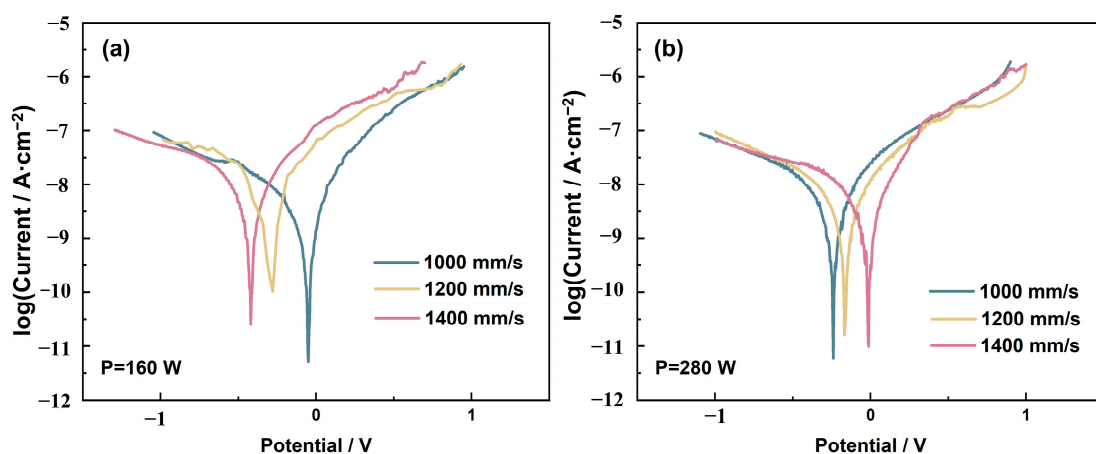


**Figure 6.** Polarization curves of Ti6Al4V alloy at laser power of (a) 160 W and (b) 280 W.

**Table 1.** Corrosion potential and current density of Ti6Al4V alloy in SBF at scanning rate of 1200 mm/s.

Laser Power/W	E <sub>corr</sub> /V	I <sub>corr</sub> /(nA·cm <sup>-2</sup> )	R <sub>p</sub> (MΩ·cm <sup>2</sup> )
160	-0.28	25.37	1.25
200	-0.09	12.21	2.73
240	-0.04	7.94	3.16
280	-0.17	9.88	2.41

**Table 2.** Corrosion potential and current density of Ti6Al4V alloy in SBF at laser power of 160 W and 280 W.

Scanning Rate/(mm/s)	160 W			280 W		
	E <sub>corr</sub> /V	I <sub>corr</sub> /(nA·cm <sup>-2</sup> )	R <sub>p</sub> (MΩ·cm <sup>2</sup> )	E <sub>corr</sub> /V	I <sub>corr</sub> /(nA·cm <sup>-2</sup> )	R <sub>p</sub> (MΩ·cm <sup>2</sup> )
1000	-0.06	15.89	2.57	-0.25	9.30	1.98
1200	-0.28	25.37	1.25	-0.17	9.88	2.41
1400	-0.41	28.76	0.87	-0.04	9.74	2.94

From Figure 6, it can be seen that when the laser power is 160 W, the E<sub>corr</sub> value gradually decreases with an increasing scanning rate owing to the increase in the unfused holes in the alloy. The I<sub>corr</sub> value increases with the increase in the scanning rate accordingly. When the laser power is 280 W, the data showed that the I<sub>corr</sub> values are approximately equal, and the E<sub>corr</sub> value increases with an increasing scanning rate that indicates that the anodic corrosion tendency of the Ti6Al4V alloys gradually reduces. Because the E<sub>corr</sub> is an indicator of the energy of the corrosion reaction, the highest value of the E<sub>corr</sub> (-0.04 V) for the scanning rate of 1400 mm/s had higher energy to be oxidized. Under the condition of the laser energy density exceeding the melting temperature of the Ti6Al4V alloy powder, an increase in the scanning rate increases the density of the specimens, which enhances the corrosion resistance. The R<sub>p</sub> of the Ti6Al4V alloys increases from 1.98 to 2.94 MΩ·cm<sup>2</sup> with an increasing scanning rate, demonstrating the greater difficulty of the electric charge to transfer through the passive film. Thus, when the laser energy density is not high enough, increasing the scanning rate cannot reduce the grain size and enhance the corrosion resistance of the alloy. The laser power is the primary parameter to be considered.

Therefore, the influence of the laser power and scanning rate on the corrosion resistance of the Ti6Al4V alloy in the process of the LPBF preparation is a dynamic adjustment process, and it is necessary to comprehensively consider the results of the interaction of the two types of parameters. Table 3 shows the contrastive analysis of the corrosion parameters in this work with the literature data for the Ti6Al4V alloy. The LPBF Ti6Al4V alloy has a better corrosion resistance than the NiTi alloy and the Ti-23Nb alloy. Meanwhile, the Ti6Al4V

alloy showed the best corrosion resistance when the scanning rate is 1200 mm/s and the laser power is 240 W.

**Table 3.** Corrosion parameters observed from potentiodynamic polarization for LPBF titanium alloys in the SBF at 37 °C.

Alloys	$E_{corr}/V$	$I_{corr}/(nA \cdot cm^{-2})$	Reference
Ti6Al4V	−0.04	7.94	this work
Ti6Al4V	$-0.369 \pm 0.008$	$15.47 \pm 4.40$	[34]
Ti6Al4V	−	73.8	[35]
Ti6Al4V	−0.144	41	[36]
NiTi	$-0.220 \pm 0.004$	$410.9 \pm 67.7$	[37]
Ti-23Nb	−	13.2	[22]

#### 4. Conclusions

The microstructure, mechanical properties, and corrosion resistance in the SBF of the Ti6Al4V alloy manufactured by LPBF under different laser power and scanning rate conditions have been investigated by the electrochemical corrosion method and mechanical tests. The main conclusions are as follows:

- (1) The microstructure of the Ti6Al4V alloy is composed of  $\alpha'$  martensite and the  $\beta$  phase. Increasing the scanning rate and decreasing the laser power decreases the transformation power from the  $\beta$  phase to the  $\alpha'$  phase and changes the morphology of the  $\alpha'$  phase from lath shaped to acicular. The hardness of the Ti6Al4V alloy reaches the maximum (480.53 HV) for a scanning rate of 1000 mm/s and a laser power of 280 W, owing to the sufficient precipitation of the  $\alpha'$  phase.
- (2) Unfused holes occur in the titanium alloy when the laser energy density is too low to melt the powder. Pores occur when the laser energy density is too high to vaporize the powder. Both defects reduce the compressive strength of the alloy. The maximum relative density of the Ti6Al4V alloy is 99.96% for a scanning rate of 1200 mm/s and laser power of 240 W, and the compressive strength reached the maximum (1964 MPa).
- (3) The influence of the laser power and scanning rate on the corrosion resistance of the Ti6Al4V alloy in the process of the LPBF preparation is a dynamic adjustment process. The corrosion resistance of an alloy can be improved effectively by increasing the scanning rate and laser power in a certain range. However, when the laser energy density is not high enough, simply increasing the scanning rate cannot reduce the grain size and enhance the corrosion resistance of the alloy. The laser power is the primary parameter to be considered. The Ti6Al4V alloy showed the best corrosion resistance when the scanning rate is 1200 mm/s and the laser power is 240 W.

**Author Contributions:** Conceptualization, Y.L.; methodology, Y.L.; software, J.T.; validation, M.W., and S.J.; formal analysis, J.T.; investigation, Y.L.; resources, Y.L.; data curation, M.W.; writing—original draft preparation, S.J.; writing—review and editing, S.J.; visualization, Y.L.; supervision, M.W.; project administration, S.J.; funding acquisition, J.Z. All authors have read and agreed to the published version of the manuscript.

**Funding:** This research was funded by the [National Natural Science Foundation of China] grant number [52004026] and the [Fundamental Research Funds for the Central Universities] grant number [FRF-TP-22-012A1].

**Data Availability Statement:** The data presented in this study are available on request from the corresponding author.

**Acknowledgments:** The helpful comments, suggestions, and encouragement from the editors and anonymous reviewers are gratefully acknowledged.

**Conflicts of Interest:** The authors declare no conflict of interest.

## References

- Gao, Y.K. Influence of different surface modification treatments on surface integrity and fatigue performance of Ti6Al4V titanium alloy. *Acta Metall. Sin.* **2016**, *52*, 915.
- Ji, S.D.; Wen, Q.; Ma, L. Microstructure along thickness direction of friction stir welded Ti6Al4V titanium alloy joint. *Acta Metall. Sin.* **2015**, *51*, 1391.
- Lu, S.L.; Qian, M.; Tang, H.P.; Yan, M.; Wang, J.; St John, D.H. Massive transformation in Ti-6Al-4V additively manufactured by selective electron beam melting. *Acta Mater.* **2016**, *104*, 303. [[CrossRef](#)]
- Tan, X.P.; Kok, Y.; Tan, Y.J.; Descoins, M.; Mangelinck, D.; Tor, S.B.; Leong, K.F.; Chua, C.K. Graded microstructure and mechanical properties of additive manufactured Ti-6Al-4V via electron beam melting. *Acta Mater.* **2015**, *97*, 1. [[CrossRef](#)]
- Mozaffar, M.; Ndip-Agbor, E.; Lin, S.; Wagner, G.J.; Ehmann, K.; Cao, J. Acceleration strategies for explicit finite element analysis of metal powder-based additive manufacturing processes using graphical processing units. *Comput. Mech.* **2019**, *64*, 879. [[CrossRef](#)]
- Deng, H.; Chen, Y.; Jia, Y.; Pang, Y.; Zhang, T.; Wang, S.; Yin, L. Microstructure and mechanical properties of dissimilar NiTi/Ti6Al4V joints via back-heating assisted friction stir welding. *J. Manuf. Process.* **2021**, *64*, 379. [[CrossRef](#)]
- Suo, H.B.; Chen, Z.Y.; Liu, J.R.; Gong, S.; Xiao, J. Microstructure and mechanical properties of Ti-6Al-4V by electron beam rapid manufacturing. *Rare Met. Mater. Eng.* **2014**, *43*, 780. [[CrossRef](#)]
- Thijs, L.; Verhaeghe, F.; Craeghs, T.; Van Humbeeck, J.; Kruth, J.-P. A study of the microstructural evolution during selective laser melting of Ti-6Al-4V. *Acta Mater.* **2010**, *58*, 3303. [[CrossRef](#)]
- Liu, Z.; Zhao, Z.B.; Liu, J.R.; Wang, L.; Yang, G.; Gong, S.; Wang, Q.; Yang, R. Microstructure and mechanical properties of Ti-6Al-4V alloy produced by electron beam fabrication. *Mater. Sci. Eng. A* **2019**, *742*, 508. [[CrossRef](#)]
- Yang, Y.; Gong, Y.; Li, C.; Wen, X.; Sun, J. Mechanical performance of 316 L stainless steel by hybrid directed energy deposition and thermal milling process. *J. Mater. Process. Technol.* **2021**, *291*, 117023. [[CrossRef](#)]
- Abedi, H.R.; Hanzaki, A.Z.; Azami, M.; Kahnouji, M.; Rahmatabadi, D. The high temperature flow behavior of additively manufactured Inconel 625 superalloy. *Mater. Res. Express* **2019**, *6*, 116514. [[CrossRef](#)]
- Shang, J.Y.; Zhan, P.; Jiang, C.; Zou, Y.; Liu, H.; Zhang, B.; Dai, M. Inhibitory effects of lanthanum chloride on wear particle-induced osteolysis in a mouse calvarial model. *Biol. Trace. Elem. Res.* **2016**, *169*, 303. [[CrossRef](#)]
- Lu, Y.; Yang, C.; Liu, Y.; Yang, K.; Lin, J. Characterization of lattice defects and tensile deformation of biomedical Co29Cr9W3Cu alloy produced by selective laser melting. *Addit. Manuf.* **2019**, *30*, 100908. [[CrossRef](#)]
- Hooreweder, B.V.; Apers, Y.; Lietaert, K.; Kruth, J.-P. Improving the fatigue performance of porous metallic biomaterials produced by Selective Laser Melting. *Acta Biomater.* **2017**, *47*, 193. [[CrossRef](#)]
- Nie, X.J.; Zhang, H.; Zhu, H.H.; Hu, Z.; Ke, L.; Zeng, X. Analysis of processing parameters and characteristics of selective laser melted high strength Al-Cu-Mg alloys: From single tracks to cubic samples. *J. Mater. Process. Technol.* **2018**, *256*, 69. [[CrossRef](#)]
- Liu, Y.; Yang, Y.Q.; Wang, D. A study on the residual stress during selective laser melting (SLM) of metallic powder. *Int. J. Adv. Manuf. Technol.* **2016**, *87*, 647. [[CrossRef](#)]
- Edwards, P.; Ramulu, M. Fatigue Performance Evaluation of Selective Laser Melted Ti6Al4V. *Mater. Sci. Eng. A* **2014**, *598*, 327. [[CrossRef](#)]
- Dai, N.; Zhang, L.-C.; Zhang, J.; Chen, Q.; Wu, M. Corrosion behavior of selective laser melted Ti-6Al-4 V alloy in NaCl solution. *Corros. Sci.* **2016**, *102*, 484. [[CrossRef](#)]
- Vandenbroucke, B.; Kruth, J.P. Selective laser melting of biocompatible metals for rapid manufacturing of medical parts. *Rapid Prototyp. J.* **2007**, *13*, 196. [[CrossRef](#)]
- Song, B.; Dong, S.; Zhang, B.; Liao, H.; Coddet, C. Effects of processing parameters on microstructure and mechanical property of selective laser melted Ti6Al4V. *Mater. Des.* **2012**, *35*, 120. [[CrossRef](#)]
- Li, J.; Lin, X.; Qian, Y.H.; Huang, W. Study on Microstructure and Property of Laser Solid Forming Ti6Al4V Titanium Alloy. *Chin. J. Lasers* **2014**, *41*, 103.
- Ren, Y.; Wu, H.; Du, J.; Liu, B.; Wang, X.; Jiao, Z.; Tian, Y.; Baker, I. Effect of laser scanning speed on microstructure, tribological and corrosion behavior of Ti-23Nb alloys produced by laser metal deposition. *Mater. Charact.* **2023**, *197*, 112647. [[CrossRef](#)]
- Kürnsteiner, P.; Wilms, M.B.; Weisheit, A.; Gault, B.; Jägle, E.A.; Raabe, D. High-strength Damascus steel by additive manufacturing. *Nature* **2020**, *582*, 515. [[CrossRef](#)]
- Jiang, P.; Zhang, C.; Zhang, S.; Zhang, J.; Chen, J.; Chen, H. Additive manufacturing of novel ferritic stainless steel by selective laser melting: Role of laser scanning speed on the formability, microstructure and properties. *Opt. Laser Technol.* **2021**, *140*, 107055. [[CrossRef](#)]
- Wei, K.W.; Wang, Z.M.; Zeng, X.Y. Element loss of AZ91D magnesium alloy during selective laser melting process. *Acta Metall. Sin.* **2016**, *52*, 184.
- Gao, P.; Wei, K.W.; Yu, H.C.; Yang, J.; Wang, Z.; Zeng, X. Effect of layer thickness on microstructure and properties of Ti-5Al-2.5Sn alloy formed by selective laser melting. *Acta Metall. Sin.* **2018**, *54*, 999.
- Alphons, A.A. *Microstructure, Texture and Mechanical Property Evolution during Additive Manufacturing of Ti6Al4V Alloy for Aerospace Applications*; The University of Manchester: Manchester, UK, 2012; Volume 61.
- Ahmed, T.; Rack, H.J. Phase transformations during cooling in  $\alpha + \beta$  titanium alloys. *Mater. Sci. Eng.* **1998**, *A243*, 206. [[CrossRef](#)]
- Gong, H.J.; Rafi, K.; Gu, H.F.; Ram, G.D.J.; Starr, T.; Stucker, B. Influence of defects on mechanical properties of Ti-6Al-4 V components produced by selective laser melting and electron beam melting. *Mater. Des.* **2015**, *86*, 545. [[CrossRef](#)]

30. Roehling, J.D.; Smith, W.L.; Roehling, T.T.; Vrancken, B.; Guss, G.M.; McKeown, J.T.; Hill, M.R.; Matthews, M.J. Reducing residual stress by selective large-area diode surface heating during laser powder bed fusion additive manufacturing. *Addit. Manuf.* **2019**, *28*, 228. [[CrossRef](#)]
31. Zhao, M.Q.; Lei, A.L. *Corrosion and Protection of Metals*; National Defense Industry Press: Beijing, China, 2002; Volume 9.
32. Huang, R.; Han, Y. The effect of SMAT-induced grain refinement and dislocations on the corrosion behavior of Ti–25Nb–3Mo–3Zr–2Sn alloy. *Mater. Sci. Eng. C* **2013**, *33*, 2353. [[CrossRef](#)]
33. Ralston, K.; Birbilis, N.; Davies, C. Revealing the relationship between grain size and corrosion rate of metals. *Scr. Mater.* **2010**, *63*, 1201. [[CrossRef](#)]
34. Wu, Y.C.; Kuo, C.N.; Chung, Y.C.; Ng, C.H.; Huang, J.C. Effects of Electropolishing on Mechanical Properties and Bio-Corrosion of Ti6Al4V Fabricated by Electron Beam Melting Additive Manufacturing. *Materials* **2019**, *12*, 1466. [[CrossRef](#)] [[PubMed](#)]
35. Gong, Y.; Wu, M.; Miao, X.; Cui, C. Effect of laser power on corrosion behavior of GO/Ti-6Al-4V coating in simulated body fluid solution. *J. Laser Appl.* **2022**, *34*, 22004. [[CrossRef](#)]
36. Avinash, D.; Leo Kumar, S.P. Investigations on corrosion resistance behavior in micro-milling of Ti-6Al-4V and Ti-6Al-7Nb alloy: A comparative study. *J. Mech. Sci. Technol.* **2020**, *34*, 1. [[CrossRef](#)]
37. Hu, J.; Ren, Y.; Huang, Q.; He, H.; Liang, L.; Liu, J.; Li, R.; Wu, H. Microstructure and Corrosion Behavior of Ti-Nb Coatings on NiTi Substrate Fabricated by Laser Cladding. *Coatings* **2021**, *11*, 597. [[CrossRef](#)]

**Disclaimer/Publisher's Note:** The statements, opinions and data contained in all publications are solely those of the individual author(s) and contributor(s) and not of MDPI and/or the editor(s). MDPI and/or the editor(s) disclaim responsibility for any injury to people or property resulting from any ideas, methods, instructions or products referred to in the content.